

ABSTRACT

Investigation of Electrically-Induced Light Emission in Epsilon Near Zero (ENZ) Heterostructure

Md Kazi Rokunuzzaman, M.S.

Co-mentor: Dr. Zhenrong Zhang

Co-Mentor: Dr. Howard Lee

Electrically driven plasmonic nanostructures can generate and guide highly confined light. Light emission and the excitation of surface plasmon polaritons by inelastic electron tunneling have been shown in metal-insulator-metal heterostructures. Similar to metals, thin films of conducting oxides whose real part of permittivity (“epsilon”) goes to zero, or epsilon-near-zero (ENZ) materials, support plasmon polariton modes. In this work I study the inelastic electron tunneling and possible ENZ mode excitation and light emission from ENZ heterostructures. Indium doped tin oxide (ITO) and HfO₂ has been used as the ENZ material and insulator, respectively. When the hot electrons injected by the means of electrical biasing across the junction of the heterostructure, they will emit the extra energy in terms of photons. The photons excite the ENZ mode in the ITO and can potentially be emitted and enhanced by the surface scattering or output coupling from nanoantenna.

Investigation of Electrically-Induced Light Emission in Epsilon Near Zero (ENZ)
Heterostructure

by

Md Kazi Rokunuzzaman, B.Sc., M.Sc.

A Thesis

Approved by the Department of Physics

Dwight P. Russell, Ph.D., Chairperson

Submitted to the Graduate Faculty of
Baylor University in Partial Fulfillment of the
Requirements for the Degree
of
Master of Science

Approved by the Thesis Committee

Zhenrong Zhang, Ph.D., Chairperson

Howard Lee, Ph.D.

Kenneth T. Park, Ph.D.

Yue (Stanley) Ling, Ph.D..

Accepted by the Graduate School

May 2021

J. Larry Lyon, Ph.D., Dean

Copyright © 2021 by Md. Kazi Rokunuzzaman

All rights reserved

TABLE OF CONTENTS

LIST OF FIGURES.....	vi
LIST OF TABLES.....	ix
ACKNOWLEDGMENTS	x
DEDICATION.....	xi
CHAPTER ONE.....	1
Overview.....	1
1.1 Electrically Driven Plasmonic Light Sources.....	1
1.2 The Goal of This Research Work.....	5
CHAPTER TWO:.....	7
Background.....	7
2.1 Introduction.....	7
2.2 The Description of Optical Permittivity.....	8
2.3 Drude Model for Conducting Materials.....	10
2.4 The Unique Properties of ENZ Material.....	11
2.5 ITO as an ENZ Material.../.....	13
2.6 ENZ Photonic Devices.....	15
2.7. The Band Diagram of the ITO Based Heterostructure.....	18
CHAPTER THREE.....	21
Fabrication and Optical Characterization Of ITO/Hfo ₂ /Au ENZ Heterostructures.....	21
3.1 Fabrication of ENZ Materials.....	21
3.1.1 <i>Metal Mask and Cleaning</i>	21
3.1.2 <i>Fabrication of Bottom Au Electrodes</i>	22
3.1.3 <i>Deposition of HfO₂ by ALD</i>	25
3.2 Optical Characterization of the ITO.....	27
CHAPTER FOUR.....	29
Electrical Measurement of Au/HfO ₂ /ITO Heterostructure.....	29
4.1 Electrical Measurement.....	29
4.2 Breakdown Voltage of HfO ₂	30
4.3 The Measurement of Tunneling Current.....	33
CHAPTER FIVE.....	37
Optical Characterization, Result and Discussion.....	37
5.1 Optical Measurement.....	37

5.2. Electrical connection in optical measurement setup.....	38
5.3 Conclusions.....	42
5.3.1 <i>Expectations and Perspectives</i>	43
REFERENCES.....	44

LIST OF FIGURES

Figure 1.1 (Left) STM tip placed on a flat gold surface without nanoantenna and (right) with a cylindrical shaped nanoantenna (right). The nanoantenna height is 51 nm and diameter are 25 nm, and the gap between the STM tip and gold surface is 2 nm [5].	2
Figure 1.2 (Left) The SPP excitation coefficient enhanced by the order of 275 at 2.07V and (right) the enhancement factor changes with the diameter of the nanoantenna [5].	2
Figure 1.3 Schematic diagram of the tunneling junctions of Ag nano cubes embedded in a polymer [6]......	3
Figure 1.4. Emission spectrum at 3.2V applied bias across the tunneling junctions. The solid lines are simulated data, and the circles are measured data. The black and red is for 65 nm and 70 nm Ag cubes, respectively [7].	4
Figure 1.5 (a) Schematic diagram of the structure of the plasmonic device with tunneling junctions, (b) Schematic of the heterostructure, and (c) Band diagram of the heterostructure [9].	4
Figure 1.6 (left) The SEM image of the device, and (right) the generated light at - 1.4 V. [9].....	5
Figure 1.7 The schematic diagram of the ITO based heterostructure.	6
Figure 2.1 The real part of permittivity goes to zero at wavelength of 1200 nm.	9
Figure 2.2 Electric field enhancement for ENZ (ITO) material in the heterostructure.	11
Figure 2.3 Electric field enhancement in SiO ₂ slab at ENZ wavelength [12].	12
Figure 2.4 Absorptance 99.5% of 80 nm ITO thin films at 43.7 ⁰ incident angle [15].....	13

Figure 2.5 The ENZ wavelength and optical loss for different materials [16].....	14
Figure 2.6 (a) ENZ wavelength changes with different carrier concentration. (b) The change of imaginary part of permittivity of ITO with different carrier density.[17]	15
Figure 2.7 ITO based plasmonic slot waveguide modulator [17]	16
Figure 2.8 The modulation in the transmission spectrum against the applied voltages. (a) 0 V, (b) 1.2 V, and (c) 2V [17].	16
Figure 2.9 The modulation in the transmission spectrum against the applied voltages. (a) 0 V, (b) 1.2 V, and (c) 2V [18].	17
Figure 2.10 The transmission spectra against the voltage (a) The transmission spectrum span from 1220 to 2250 nm at different voltage., (b) The modulation in different waveguide length and with our ITO (red square)[18]	17
Figure 2.11 Schematic of the band diagram of ENZ heterostructure.	19
Figure 3.1 The design of the metal mask.	21
Figure 3.2 The schematic diagram of fabrication step.	22
Figure 3.3 (left)The vacuum chamber of the sputtering machine and (right) entire sputtering machine set up.	24
Figure 3.4 (Left) The profilometry measurement of top right Au electrode, and (right) the schematic diagram of the sample.	24
Figure 3.5 The ALD machine situated at Lee nano-optics lab at Baylor science building.	26
Figure 3.6 (Left) Schematic of sample with tape, (middle) the image of the sample with thermal tape and (right) the SEM image of 30 nm HfO ₂	26
Figure 3.7 (Left) Schematic diagram of sample and (right) the optical image of the sample.	27

Figure 3.8 Ellipsometry measured permittivity of 50 nm thick ITO thin film.....28

Figure 4.1 The probe station with Keithley-4200 semiconductor analyzer.30

Figure 4.2 The Schematic diagram with probe.....31

Figure 4.3 (left)The I-V curve of sample#1 area#1 ,and (right) area#232

Figure 4.4 Breakdown voltages corresponding to different device areas.....33

Figure 4.5 (Left) Sample#1 image of device#1, (middle) device#2, and (right) device#3.....33

Figure 4.6 The PF emission current at moderate electric field.....35

Figure 4.7 The FN tunneling current at the higher electric field.....35

Figure 5.1 Schematic diagram of the optical setup to detect the emission of light.37

Figure 5.2 (left)The picture of the optical set up, and (right) the sample with sample holder.....38

Figure 5.3 (Left) The schematic of test sample and (right) the picture of the test sample.39

Figure 5.4 The I-V curve of (a) first electrode, (b) second electrode, (c) third electrode, and (d) fourth electrode of test sample.40

Figure 5.5 The I-V curve of (a) first electrode, (b) second electrode, and (c) third electrode of test sample by Keithley-2450 with Ag paste.....41

LIST OF TABLES

Table 3.1 The ENZ wavelength of ITO measured by ellipsometry.....	29
Table 4.1 The Breakdown voltages of different areas of various samples.....	33
Table 5.1 Measurement with Probe Station.....	40
Table 5.2 Measurement with Keithley-2450.....	42

ACKNOWLEDGMENTS

First, I would like to thank Dr. Howard Lee for supervising and giving the opportunity to work on this research project. We started this project right before the pandemic began. Moreover, he was also in transition period from Baylor university to University of California, Irvine. Despite all these obstacles his continuous guidance and inspiration helped me to conduct this research work. I would also like to thank Dr. Zhenrong Zhang for serving as my co-advisor. My gratitude also goes to Dr. Kenneth T. Park and Dr. Yue (Stanley) Ling for serving as the members of my thesis committee.

I thank to Dr. Peinan Ni for helping me to initiate the research project. I must thank Dr. Oleksiy Anopchenko for his cooperation and help to understand the important concept regarding this research project. I also thank to Khant Minn, Sudip Gurung, Indra Ghimire, Jay Joyner, and Michel Schell along with all the group members of “Lee Nano-optics Lab”. Finally, my cordial gratitude to my friend Syeed Mahedi Hasan for borrowing his car to travel from my apartment to BRIC.

DEDICATION

To my parents

CHAPTER ONE

Overview

Light-emitting diodes (LEDs) and lasers are traditional sources of light. Electrically driven plasmonic nanostructures can also generate and guide highly-confined light. In this chapter, I will present an overview of the electrically driven plasmonic light sources and describe the goal of my research work.

1.1 Electrically Driven Plasmonic Light Sources

In the recent years, several studies have been reported on electrically driven surface plasmon polariton (SPP) excitation. For example, electrical excitation of SPP has been demonstrated using integrated organic light emitting diodes (OLEDs) [1], nano-LEDs [2-3], and silicon nanocrystals [4]. Electrical excitation of SPP could lead to direct integration of nano-sources of light in nano-photonics circuits.

Also, light emission by inelastic electron tunneling has been used to generate SPP. This process is inefficient and can be enhanced by a proper design of the plasmonic nanostructures. Therefore, with the advancement of nano-fabrication methods, we can make different plasmonic structures to efficiently excite SPP by using electron tunneling.

In 2016, F. Bigourdan *et al.* theoretically studied the excitation of SPP mode by inelastic electron tunneling between a tip of the scanning tunneling microscope (STM) and gold surface [5]. In this work, enhanced generation of SPP propagating along gold-air interface was shown by using a resonant nanoantenna under the STM tip (Fig. 1.1). A large enhancement in the radiative efficiency of the nanoantenna and electric field in the

gap between the STM tip and the nanoantenna led to an enhancement factor of 275 of SPP excitation (Fig. 1.2).

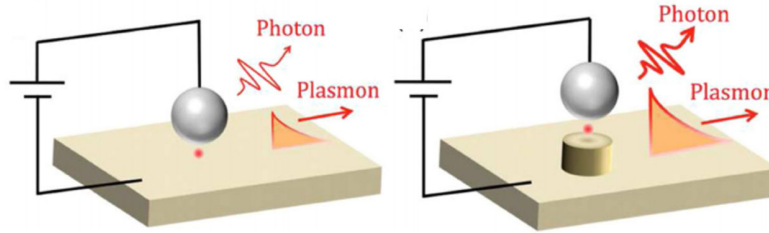


Figure 1.1 (Left) STM tip placed on a flat gold surface without nanoantenna and (right) with a cylindrical shaped nanoantenna (right). The nanoantenna height is 51 nm and diameter are 25 nm, and the gap between the STM tip and gold surface is 2 nm [5].

The metal and air create interface to support SPP mode. With cylinder shaped nanoantenna they showed the SPP excitation coefficient enhanced by a factor of 275 Fig 1.2.(left).

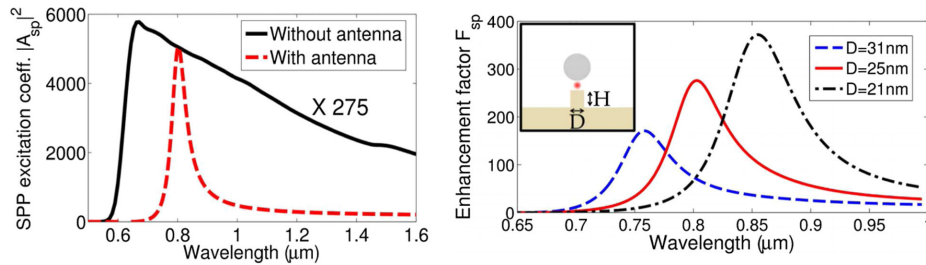


Figure 1.2 (Left) The SPP excitation coefficient enhanced by the order of 275 at 2.07V and (right) the enhancement factor changes with the diameter of the nanoantenna [5].

A control over the emitted spectrum was shown too (Fig. 1.2). From this figure, we also can see the spectrum becomes narrower compared to spectrum without antenna. In the Fig. 1.2 (right), change of enhancement factor with the diameter of the nanoantenna has been demonstrated which facilitates us to tune the emitted spectrum. In 2018 H. Qian *et al.* experimentally demonstrated the electrically-induced light emission

by using Ag nanocrystals assembled into a metal-insulator-metal (MIM) heterostructure (Fig. 1.3) [6].

In 2018 H. Qian *et al.* experimentally demonstrated the electrically-induced light emission by using Ag nanocrystals assembled into a metal-insulator-metal (MIM) heterostructure [6]. As shown in Fig. 1.4, measured far field light emission with efficiency by 2% at near-IR frequencies can be observed [7,8].

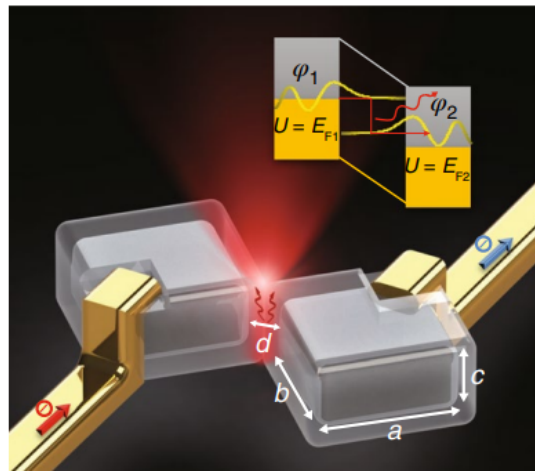


Figure 1.3 Schematic diagram of the tunneling junctions of Ag nano cubes embedded in a polymer [6].

With 3.2 V applied bias throughout the tunneling junctions they found the emission spectrum shows agreement between the simulated and experimental results. They also showed by changing the Ag nano cubes height the emission spectrum changes, suggesting the tunability of the emission spectrum.

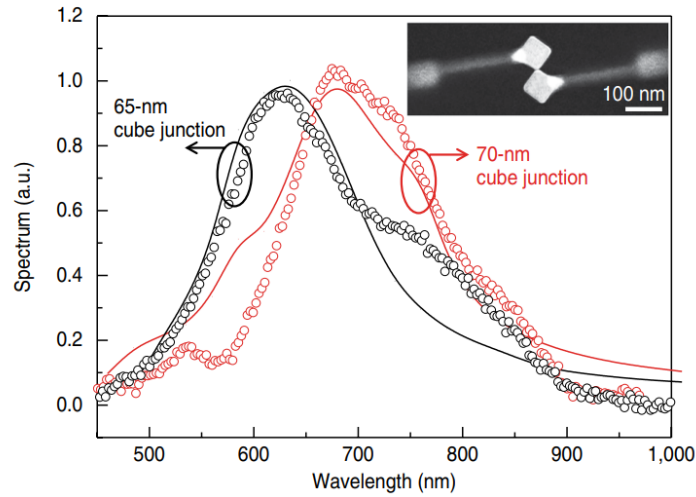


Figure 1.4. Emission spectrum at 3.2V applied bias across the tunneling junctions. The solid lines are simulated data, and the circles are measured data. The black and red is for 65 nm and 70 nm Ag cubes, respectively [7].

W. Du *et al.* demonstrated excitation of SPP from a MIM structure by electrical means [9]. In their work they have fabricated glass/Al/Al₂O₃/Au heterostructure to excite the SPP by electrical tunneling. Figure 1.5 shows the schematic diagram of the structure of the device and heterostructure and the band structure.

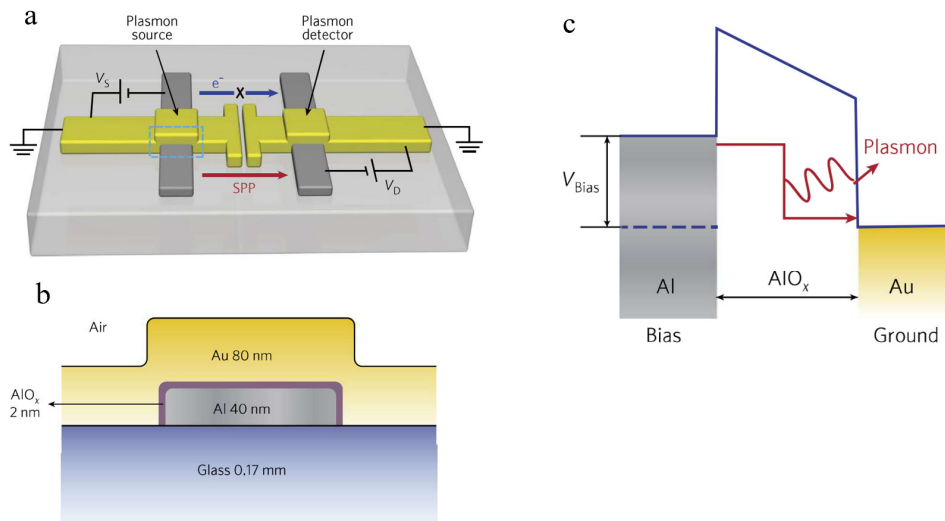


Figure 1.5 (a) Schematic diagram of the structure of the plasmonic device with tunneling junctions, (b) Schematic of the heterostructure, and (c) Band diagram of the heterostructure [9].

The thickness of the Al, Al₂O₃, and Au is 40 nm, 2nm, and 80 nm, respectively. When they applied the electrical bias to the Al electrode by keeping the Au electrode grounded, a depletion region formed due to the difference in the fermi level of the two metal layers. When the electron tunnels through the insulating layer towards the Au electrode, the electron will emit the extra energy that will excite the SPP mode in the MI interface. They used two similar devices, one is the plasmon source and the other one is plasmon detector. There is a gap of 200 nm in between the source and plasmon detector device. This gap will allow the SPP to propagate from the plasmon source to detector. Generation of light has been shown in these MIM structures at electrical bias of -1.4 V (Fig. 1.6 (b))

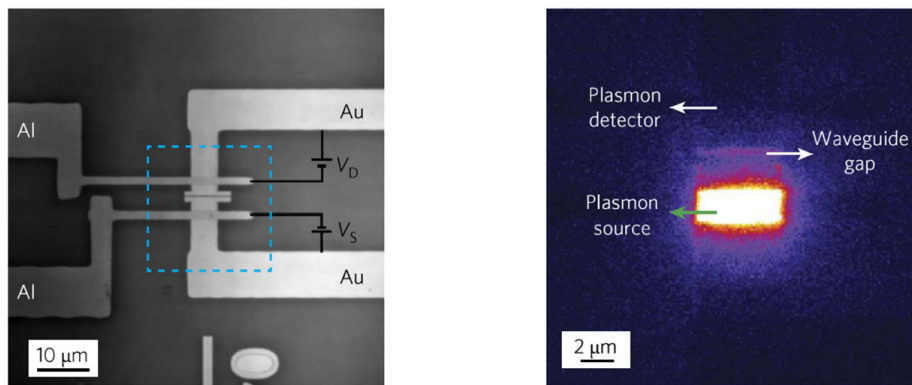


Figure 1.6 (left) The SEM image of the device, and (right) the generated light at -1.4 V. [9]

1.2 The Goal of This Research Work

The above studies on excitation of SPP by electrical means show the initial demonstrations on developing light source in nanoscale plasmonic device. And the geometry of the structure can be designed to alter the emitted spectrum and emission efficiency. However, most of the current studies on electrical-generation of nano-light are limited in plasmonic metal-insulator-metal structures.

In this research work, we aim to take advantage of the unique properties of ENZ materials for the investigation of electrically induced light emission, by incorporating ITO ENZ material with the metal-insulator (MI) structure (Fig. 1.7). To excite the ENZ mode by the electrical means, glass/Au/ITO/HfO₂/Au heterostructures have been fabricated. The ITO material used in the study is a transparent conductive oxide (TCO) with high carrier concentration in the order of 10^{19} cm^{-3} and electrical tunable properties might lead to highly tunable and enhanced light emission. In the following chapters, the background of the unique properties of ENZ, fabrication of the structures, and electrical and optical characterizations of the fabricated structures will be discussed.

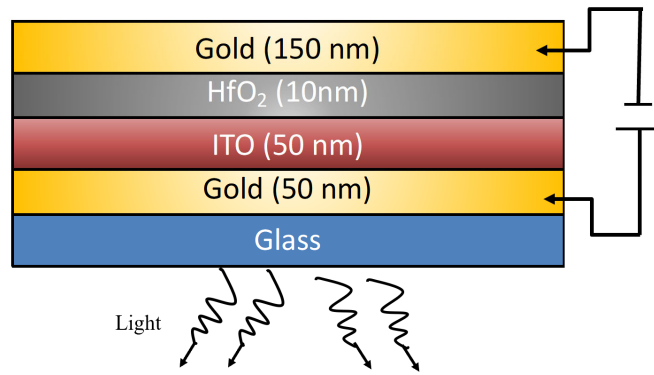


Figure 1.7 The schematic diagram of the ITO based heterostructure.

CHAPTER TWO

Background

In the 1st chapter I discussed the overview of the research project. In this chapter I will discuss the necessary background information about the research work.

2.1 Introduction

Understanding the light matter-interaction is important for manipulation and controlling the light propagation. From Maxwell's equation and electromagnetic theory, the n (refractive index), ϵ (relative permittivity) and μ (relative permeability) are important physical quantities to understand the optical properties of the materials. If we can change any of these parameters of a material, then we can control light propagation and achieve the desired optical functions. Most of the materials in the optical regime shows weak magnetism and therefore, $\mu=1$ [10]. The other quantity ϵ is the factor that can be changed to achieve the desired control over light propagation. Moreover, the equation $n = \sqrt{(\epsilon\mu)}$ makes $n=0$ when the ϵ goes to zero and this physical property exhibits unprecedented phenomena which are not present in the material with large value of ϵ . The absolute permittivity, often called the permittivity of the material. It relates the two quantities named electric field and electric displacement current. We can tailor epsilon to have positive, negative or zero value, and hence inducing extraordinary optical characteristics for various applications [10].

2.2 The Description of Optical Permittivity

The dispersion relation of metal and electromagnetic wave can be derived from the classical framework of Maxwell's equations. From the macroscopic electromagnetism equation of Maxwell's equations.

$$\Delta \cdot D = \rho_{ext} \dots \dots \dots (1.3a)$$

$$\Delta \cdot B = 0 \dots \dots \dots (1.3b)$$

$$\Delta \times E = -\frac{\partial B}{\partial t} \dots \dots \dots (1.3c)$$

$$\Delta \times H = J_{ext} + \frac{\partial D}{\partial t} \dots \dots \dots (1.3d)$$

where, D = dielectric displacement current, B = magnetic flux density, E = electric field, H = magnetic field, ρ_{ext} = external charge density, J_{ext} = external current density.

Follow the mathematical derivation in standard electromagnetic theory, we obtain the relation in between relative permittivity or dielectric function and conductivity [13].

$$\varepsilon(K, w) = 1 + \frac{i\sigma(K,w)}{\varepsilon_0 w} \dots \dots \dots (1.3e)$$

where, K = wave vector, w = angular frequency, σ =conductivity, ε and σ depicted the bound charges and free charges contribution, respectively. The equation of complex dielectric function.

$$\varepsilon(w) = \varepsilon_1(w) + i\varepsilon_2(w) \dots \dots \dots (1.3f)$$

where, $\varepsilon_1(w)$ = real part of permittivity, $\varepsilon_2(w)$ =imaginary part of permittivity

The permittivity can be gained from the refractivity equation:

$$n(w) = n(w) + ik(w) \dots \dots \dots (1.3g)$$

After separating the real and imaginary part

$$\epsilon_1 = n^2 - k^2 \dots \dots \dots (1.3h)$$

$$\epsilon_2 = 2nk \dots \dots \dots (1.3i)$$

When the real part of permittivity in equation (1.3g) goes to zero, it is so-called epsilon-near-zero (ENZ) regime. Fig. 2.1 shows an example of the permittivity vs wavelength relation of a 80 nm-thick ITO thin film (real part of ϵ in blue and imaginary part of ϵ in pink dashed). This ITO thin film was fabricated by RF magnetron sputtering on the silicon substrate. The real part of ϵ goes to zero at wavelength of 1200 nm and this is the ENZ wavelength of ITO. Below the ENZ point, the ITO shows dielectric characteristic and above ENZ point it shows metallic characteristic.

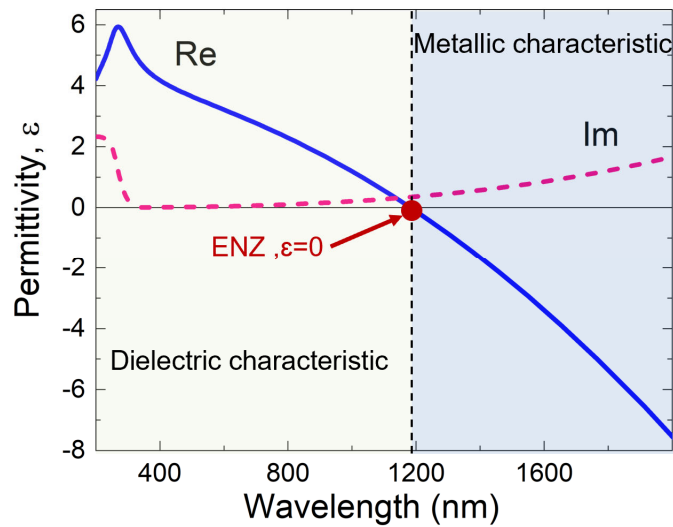


Figure 2.1 The real part of permittivity goes to zero at wavelength of 1200 nm.

2.3 Drude Model for Conducting Materials

The optical properties of metals or TCO materials can be explained by plasma model. In the plasma model free electrons are considered as a gas with number density n . After applying the electric field, the electrons oscillate. The motion of the electrons is damped harmonic. The damping coefficient is $\gamma=1/\tau$. Where, τ is known as relaxation time. At room temperature $\tau=10^{-14}$ s and $\gamma=100$ THz [11].

The equation of motion of electron of plasma sea is.

$$m \frac{d^2x}{dt^2} + m\gamma \frac{dx}{dt} = -eE \dots \dots \dots (1.3j)$$

where, E is the electric field and e is the electron charge. If we consider the harmonic dependence for solution

$$E(t) = E_0 e^{-i\omega t} \text{ for the field and} \dots \dots (1.3k)$$

$$x(t) = x_0 e^{-i\omega t} \text{ for displacement}$$

By putting (1.3k) in (1.3j) we will get the displacement

$$x(t) = \frac{e}{m(\omega^2 + i\gamma\omega)} E(t) \dots \dots \dots (1.3l)$$

By using polarization $P = -nex$ we will get

$$D = \epsilon_0 \left(1 - \frac{\omega_p^2}{\omega^2 + i\gamma\omega} \right) E \dots \dots \dots (1.3m)$$

where $\omega_p^2 = \frac{ne^2}{\epsilon_0 m}$ is the plasma frequency . Finally, the dielectric function of the free electron gas is.

$$\varepsilon(\omega) = 1 - \frac{\omega_p^2}{\omega^2 + i\omega\gamma} \dots \dots \dots (1.3n)$$

Equation (1.3n) known as the Drude model.

2.4 The Unique Properties of ENZ Material

ENZ materials have exhibited extraordinary optical properties. These unique properties enable the researchers to design novel photonic devices with advanced functionalities. Because of the vanishing ε the continuity of the normal component of the electric displacement imposes a discontinuity in the normal component of electric field. This phenomenon causes strong enhancement in the electric field. In the Fig. 2.2 electric field enhancement for ITO based has been shown. In the fig the light incidents on the high-index substrate. When the light reaches the edge of the ENZ material. The ENZ material is ITO and the electric field enhanced by 23 times in the edge. The field enhancement continues until the other edge of the ITO. It is also can be seen from the graph the electric field is almost constant throughout the ITO. The position on the vertical axes is normalized to the ITO thickness.

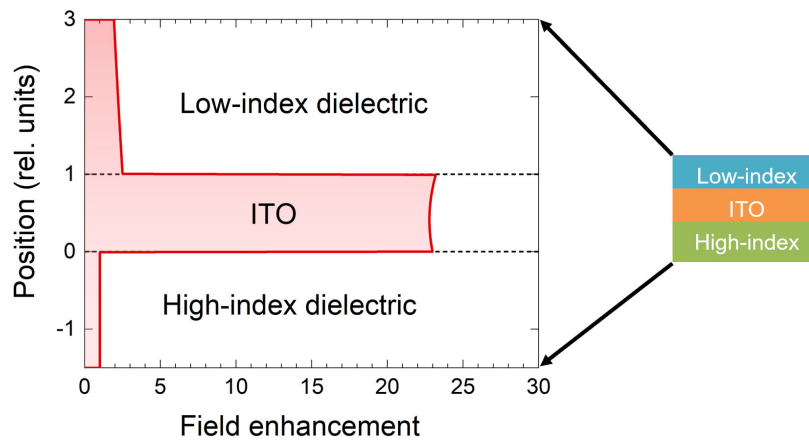


Figure 2.2 Electric field enhancement for ENZ (ITO) material in the heterostructure.

In 2013, S. Campione *et.al* [12] investigated a 400 nm thick SiO₂ slab surrounded by free space ($\epsilon=1$). SiO₂ is a naturally occurred ENZ material and its ENZ wavelength at 37 THz. At the ENZ wavelength the electric field enhancement yields 3.5 times which depicted in Fig. 2.3.

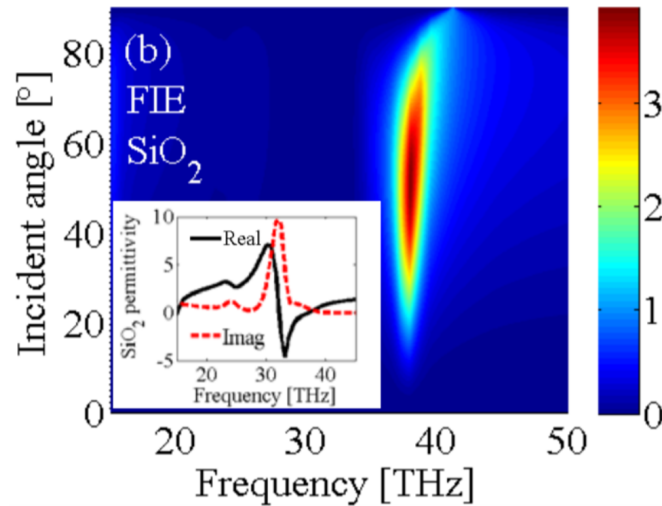


Figure 2.3 Electric field enhancement in SiO₂ slab at ENZ wavelength [12].

Another unique property of ENZ materials is perfect absorption (PA). At the ENZ wavelength normal component of electric field becomes very strong. This strong electric field can lead to perfect absorption [13,14]. A. Anopchenko *et al.* in 2018 excite the ENZ mode in RF magnetron sputtered ITO thin films with Kretschmann-Raether configuration [15]. Thickness of the of ITO nanolayers were 80 nm. At incident angle 43.7 degree, they observed resonant dip (red) in the reflectivity depicted the ENZ absorption of 99.5% as shown in the Fig. 2.4. Other than strong electric field enhancement and absorption. ENZ materials also find unique potential applications include thin film perfect absorbers/isolators, efficient nonlinear optical switching elements, media for enhanced

and controlled quantum emission, and electrically tunable modulator and metasurfaces. In this work, we focus on the electrically induced emission properties of the ENZ materials.

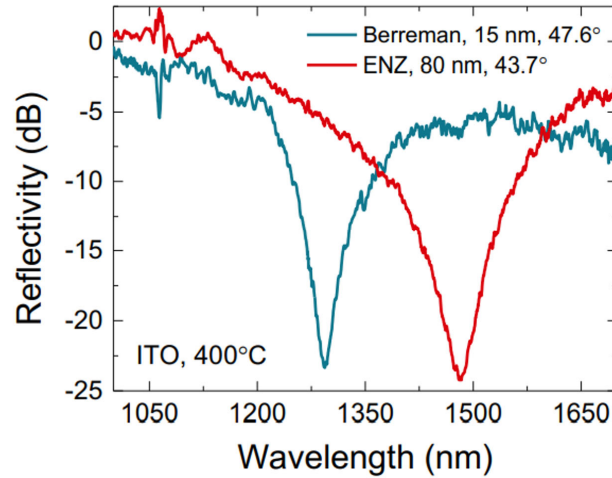


Figure 2.4 Absorptance 99.5% of 80 nm ITO thin films at 43.7° incident angle [15].

2.5 ITO as an ENZ Material

Naturally found materials such as Au and Ag they have high carrier density (10^{22} cm^{-3}). Their high carrier density leads them to show ENZ property. However, these materials have ENZ point at ultraviolet region and have high optical losses, implying obstacles to use them in visible and telecommunication wavelength and other practical optical applications. In Fig. 2.5 presents the ENZ wavelength and optical losses of different ENZ materials [16]. From the graph we can see that several materials such as metals, semi-metals, and semiconductors exhibit ENZ properties at different wavelength regime. However, some of the materials, for example TiN and TiSi, have very high optical loss (large imaginary value of permittivity). In contrast, transparent conductive oxides (TCO) such as aluminum doped zinc oxide (AZO), indium doped tin oxide (ITO) have very high carrier density in the order of 10^{19} - 10^{21} cm^{-3} due to heavily doping,

leading the ENZ wavelength located in the near infrared region that could be utilized for optical applications.

Among the TCOs, ITO has excellent properties and could be routinely fabricated by sputtering technique. Firstly, The ENZ wavelength of ITO is in the near-IR range and this range overlaps with the telecommunication band [16]. In addition, ITO has relatively low optical losses due to the low damping coefficient γ . Finally, the ENZ wavelength of ITO can be tuned by changing the carrier concentration. In Fig. 2.5 the red circle drawn on ITO on the graph and red arrows drawn to show the different ENZ wavelength. The top horizontal axes show the ENZ wavelength ITO is in the IR wavelength.

Again, in Fig. 2.6 the changes of ENZ wavelength of ITO have been presented. From this figure, we can see the ENZ point changes with the changes of the carrier concentration. Therefore, in this research work ITO has been chosen as the ENZ materials for the ENZ heterostructure.

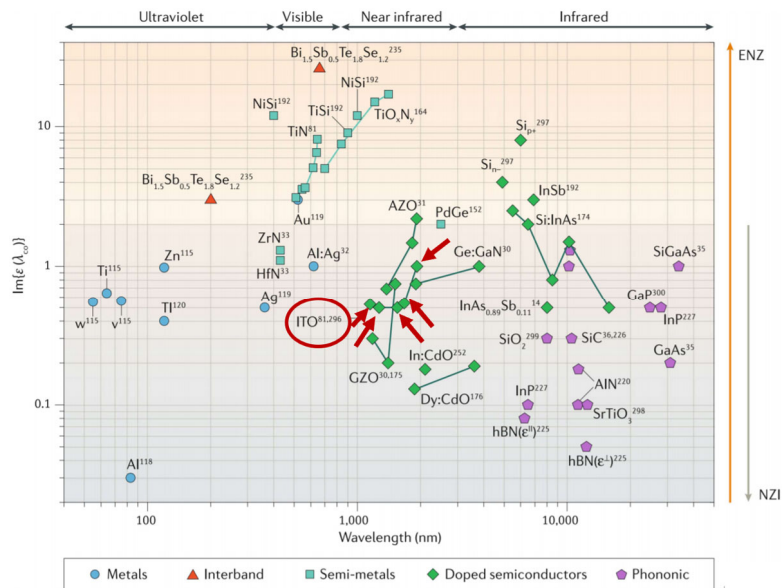


Figure 2.5 The ENZ wavelength and optical loss for different materials [16].

As shown in Fig. 2.6 (a), we can see that for different carrier concentrations of ITO, the real part of ϵ crosses the zero at different wavelengths [17]. The red marks have depicted the different points where the real part of ϵ goes to zero and the different color shows the change in the carrier concentration. With the increase of the carrier concentration of ITO, the ENZ wavelength shifted towards the shorter wavelength. Moreover, In the Fig. 2.6 (b) the imaginary part of ϵ has been presented. We can see the imaginary part of also changes with the change of carrier concentration. In our study, we will control the carrier concentration of ITO (thus the ENZ wavelength) by varying the fabrication condition (e.g. deposition temperature) during the magnetron sputtering fabrication.

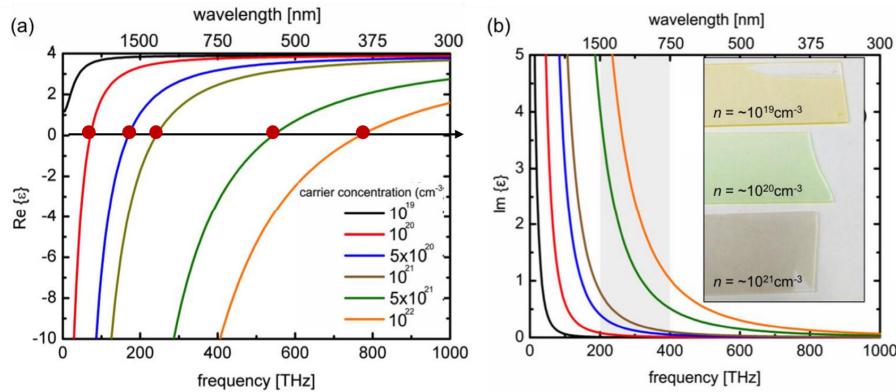


Figure 2.6 (a) ENZ wavelength changes with different carrier concentration. (b) The change of imaginary part of permittivity of ITO with different carrier density.[17]

2.6 ENZ Photonic Devices

ENZ materials have been used to develop novel photonic devices. ENZ materials can manipulate phase and amplitude more effectively than conventional photonic devices. In recent years, an excellent progress made in integrated ENZ photonic devices. In 2014, H. W. Lee *et al.* demonstrated modulation of transmission spectrum of ITO

based plasmonic slot waveguides (Fig. 2.7) [17]. In their research work, they applied different voltages to the electrodes in between Au and ITO and measured the modulation on the transmission spectra.

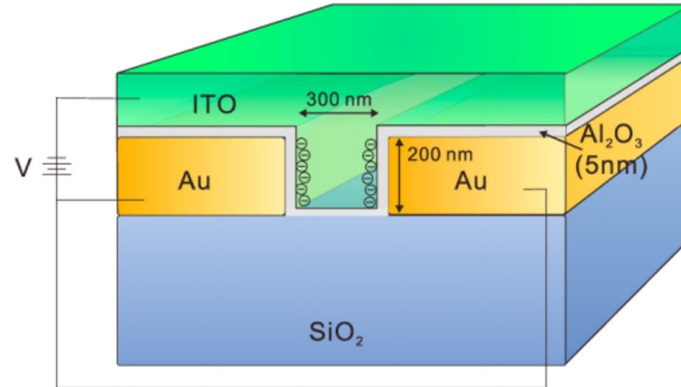


Figure 2.7 ITO based plasmonic slot waveguide modulator [17]

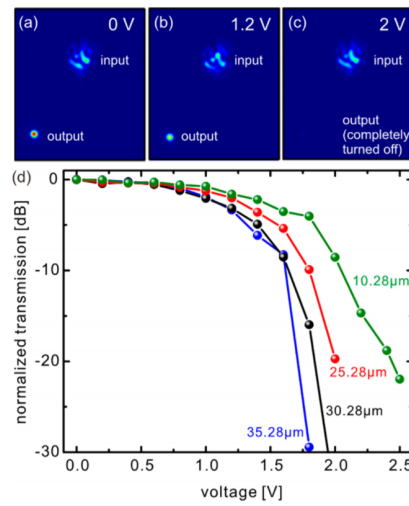


Figure 2.8 The modulation in the transmission spectrum against the applied voltages. (a) 0 V, (b) 1.2 V, and (c) 2V [17].

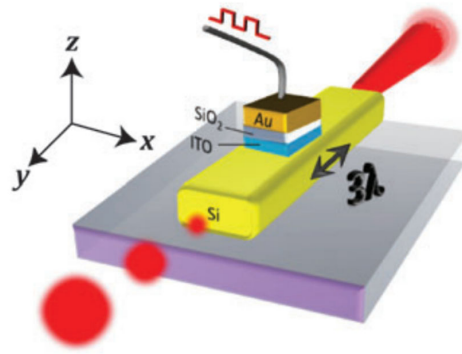


Figure 2.9 The modulation in the transmission spectrum against the applied voltages. (a) 0 V, (b) 1.2 V, and (c) 2V [18].

In another study, researchers found that applied electrical bias across the metal-oxide-semiconductor (MOS) capacitor leads to the MOS mode change the laser beam intensity. The active tunability of ITO layer helps to maximize the electric field in the center of MOS structure. In Fig. 2.10 (a) the transmission spectrum ranging from 1220 to 2200 nm. As shown in Fig. 2.10 (b), they used different length of the strip and found different transmission. This finding suggested that the absorption properties due to the formation of accumulation layer with ENZ condition in ITO could lead to significant electrical modulation of photonic mode propagation.

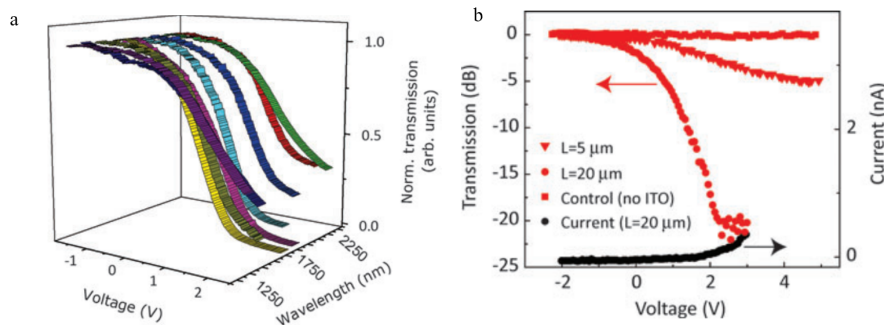


Figure 2.10 The transmission spectra against the voltage (a) The transmission spectrum span from 1220 to 2250 nm at different voltage., (b) The modulation in different waveguide length and with our ITO (red square) [18]

In the chapter one I discussed about light generation from the nanostructure and the goal of the research work. In this chapter (second chapter) I introduced the ENZ materials and their unique properties. I also showed few examples of ENZ photonic devices. In the next section of this chapter, I will discuss the band diagram of ENZ based heterostructure along with the tunneling mechanism.

2.7. The Band Diagram of the ITO Based Heterostructure.

The energy band diagram is an essential information to understand the physics of our ITO based heterostructure. The analysis of the band diagram will give us the proper understanding how the light can be generated from the corresponding heterostructure. Let us discuss the band diagram first. The schematic band diagram of ITO/HfO₂/Au heterostructure has been depicted in Fig. 2.11. In the figure, $E_{F,Au}$, $E_{F,ITO}$, $E_{C,ITO}$, and $E_{V,ITO}$ represent the Fermi level of Au, Fermi level of ITO, conduction band of ITO, and the valence band of ITO, respectively. We know that ITO is a degenerated or highly doped semiconductor. Eventually, the band diagram of the heterostructure will be similar to the band structure of metal-oxide-semiconductor (M-O-S).

In the figure the band diagram has been depicted with the applied bias. $\phi_{Barrier}$ represents the barrier height in between the Fermi level of metal (Au) and conduction band of insulator (HfO₂) layer. After applying the bias at the Au electrode, the Fermi level of Au will move in upward direction due to injecting of electrons. The Fermi level of Au depicted by red line in the band diagram. To maintain the electron affinity constant of HfO₂, there will be a bending in the conduction band of HfO₂ which has been depicted by blue line. Electron affinity can be defined by the difference in between vacuum level energy and the conduction band of a material. Usually, this property is constant for all materials.

Again, for keeping the electron affinity constant of ITO layer the conduction band will bend. and create a depletion region at the interface (HfO₂-ITO). The bending of conduction band has been depicted by the green line in the figure. The depletion region will decrease if we move away from the interface (HfO₂-ITO) After passing the significant distance from the interface the depletion region vanishes, and the conduction band of ITO retain the straight-line shape.

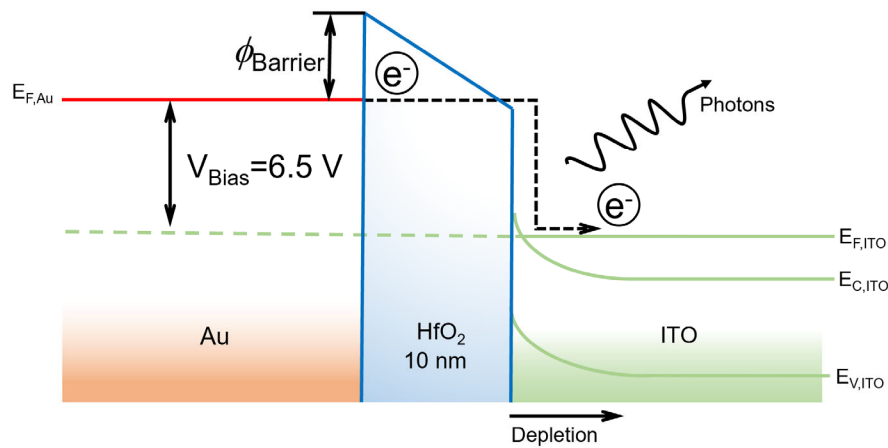


Figure 2.11 Schematic of the band diagram of ENZ heterostructure.

Now let us see how the electron will tunnel and excite the ENZ mode of ITO. When the bias (6.5V) will be applied at the Au electrode. The applied bias is the difference in between Fermi level of Au and ITO. Due to the difference of Fermi levels, electron will go to a lower state after tunneling through the insulator (HfO₂) layer. When the electron goes from higher state to lower state, it releases the extra energy. In our case the extra energy of electron will be released in term of photons. Finally, the photons excite the ENZ mode in the ITO and can potentially be emitted and enhanced by the surface scattering or output coupling of nanoantenna. The applied bias has been calculated from Fowler-Nordheim (FN) tunneling mechanism. In section 4.3, the detailed

calculation has been presented. The barrier height is also calculated from the FN tunneling mechanism and it is 2.7 eV.

CHAPTER THREE

Fabrication and Optical Characterization of ITO/HfO₂/Au ENZ Heterostructures

3.1 Fabrication of ENZ Materials

3.1.1 Metal Mask and Cleaning

Magnetron Sputtering and atomic layer deposition (ALD) techniques have been used to deposit the ENZ materials and metals on the substrate. Before starting the deposition, 1 cm by 1 cm metal masks were designed by AutoCAD for depositing with selected areas (Fig. 3.1). In the design, the square shaped head worked as the electrode pad to apply voltages and all the four pads are similar in area. There are 4 long stripes connecting the square pads. Unlike the electrode pads the stripes are not similar in length and width to make different active areas of the devices.

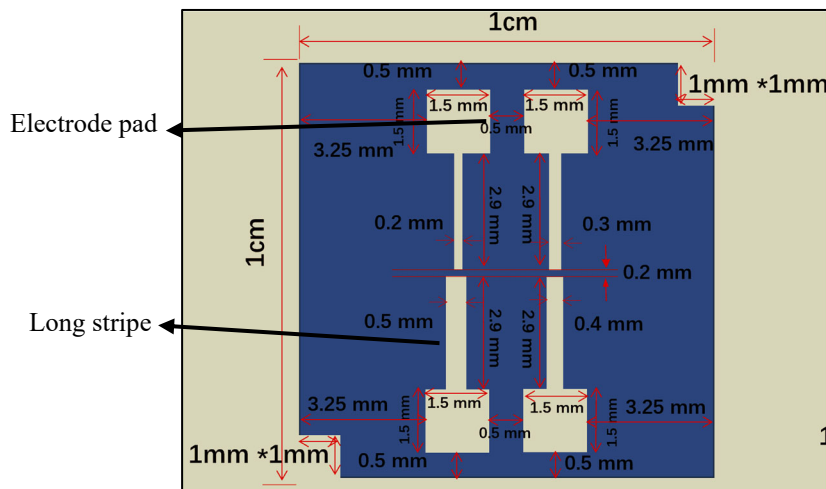


Figure 3.1 The design of the metal mask.

The entire fabrication process has been divided into 5 steps and the steps are shown in Fig. 3.2. At the very first step of the fabrication, the glass substrates were cleaned in three steps. At the first step the glass substrates were sonicated for 15 mins by acetone and then 15 mins by isopropyl alcohol (IPA). For the final step of cleaning, all the substrates were rinsing with distilled water (DI). The same cleaning treatment process was followed to clean the masks.

3.1.2 Fabrication of Bottom Au Electrodes

The first step of Au electrodes was fabricated by magnetron sputtering. Magnetron sputtering is a plasma-based technique, and it works at high vacuum pressure condition where the plasma is generated from the target. There are several types of targets are used for deposition.

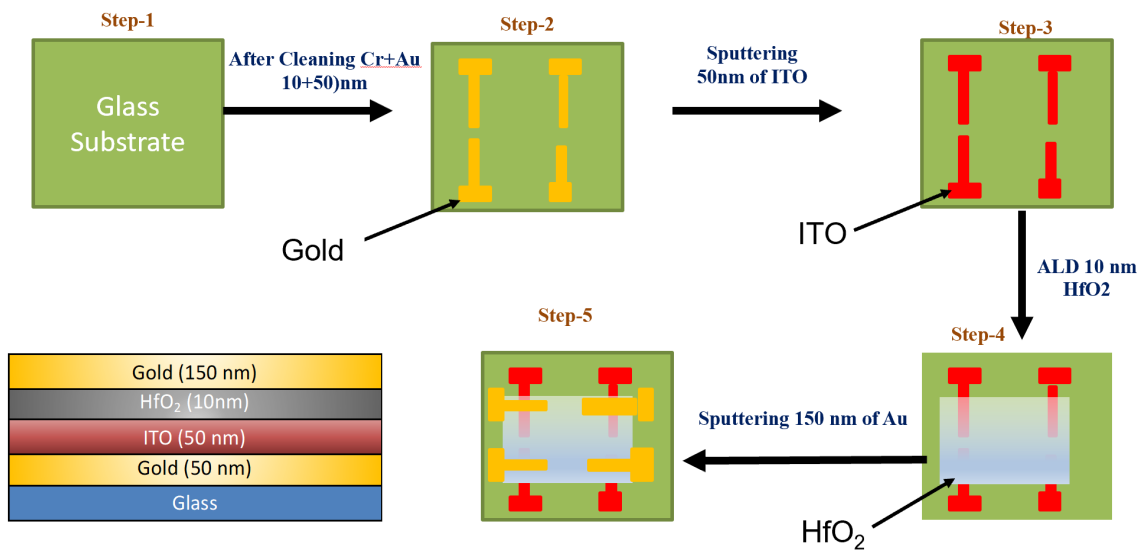


Figure 3.2 The schematic diagram of fabrication step.

Magnetron sputtering machine (Fig. 3.3) situated at BRIC facility of Baylor University was used for the fabrication. It has three power sources named RF-1, RF-2, and DC power with 3 guns. After substrates were cleaned, they were placed in the sample holder of magnetron sputtering for Au deposition. To make sure Au stick to the glass substrate properly, 10nm of chromium (Cr) was deposited before Au. The Cr layer was fabricated with 50W DC current and room temperature. The rotation speed was 5 rpm. Pre-deposition time was 15 seconds to make sure the plasma was igniting from the target. The deposition time was 60 seconds. Immediately after the Cr deposition, 50 nm of Au was deposited with the same alignment of the metal mask by using the 25W DC power and keeping the other deposition condition the same. The pre-deposition time for the Au was 40 seconds and the deposition time was 300 seconds. Extra samples are deposited on bare glass substrate for profilometry characterization.

The profilometer located in the cleanroom of the BRIC facility were used to ensure the thickness of the Au. After several measurements, thickness of Au is ~50 nm was confirmed, which ensured the Au was deposited correctly. Figure 3.4 depicts the profilometry measurement of one of the samples.

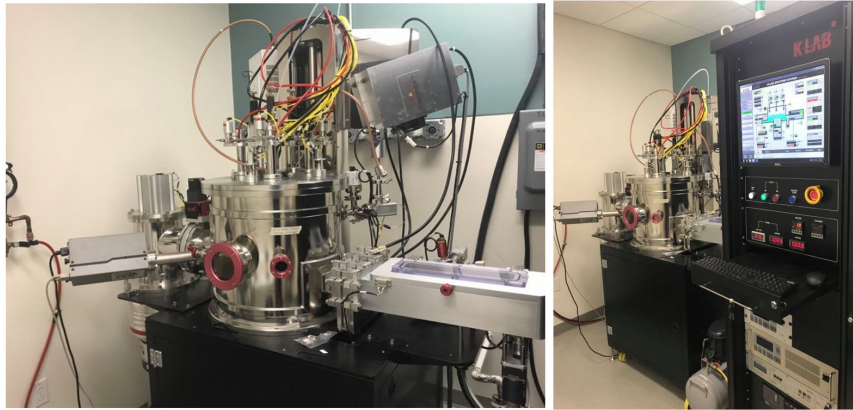


Figure 3.3 (left)The vacuum chamber of the sputtering machine and (right) entire sputtering machine set up.

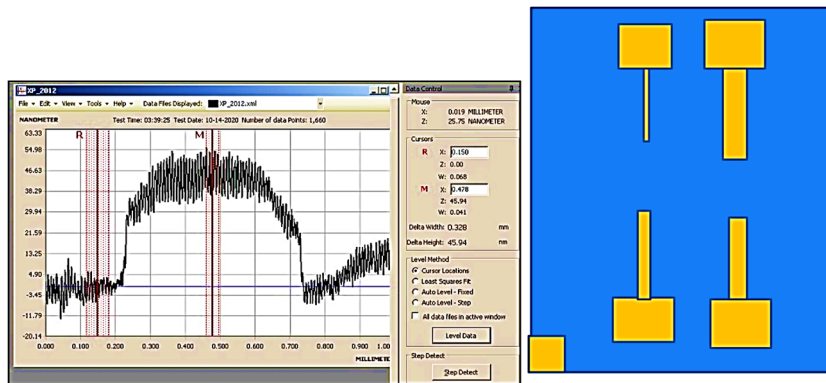


Figure 3.4 (Left) The profilometry measurement of top right Au electrode, and (right) the schematic diagram of the sample.

At the 3rd step, 50 nm of ITO was deposited using magnetron sputtering. Before the deposition, the metal masks were sonicated in acetone and IPA. To maintain the same alignment of the Au electrode, the same metal masks were used. ITO was deposited by using the ITO target which was installed in the third gun of the machine at 300 degree Celsius. High deposition temperature of 300 °C was used to make sure the high doping concentration of ITO. 100W AC power source was used, and the other conditions were similar to the deposition of Au. The preposition time was 45 seconds and after the plasma

generation from the ITO target, the main shutter was opened for the deposition for 600 seconds. Bare glass was also used as a reference to make sure the thickness of ITO was 50 nm. From the profilometry measurements, the ITO was found to be deposited properly with correct thickness.

3.1.3 Deposition of HfO₂ by ALD

At the 4th step of deposition (Fig. 3.2), ALD machine which is situated at Lee nano-optics lab in the BSB building of Baylor university was used to deposit the insulating layer HfO₂ (Fig. 3.5). ALD is a deposition technique which is known to deposit high-k thin films such as HfO₂ and Al₂O₃. This is a chemical process which is used sequential deposition of gas phase in the substrate. Before deposition, the glass/Cr-Au/ITO structures were cleaned with N₂ flow to make sure the surface of the structures was free of dust. The surface of the structures was checked by the optical microscope to make sure the electrodes are not damaged by any scratches.

Thermal tape was used to cover the electrode pads to avoid any HfO₂ material deposited on the electrode pads. Fig. 3.6 shows the schematic of the samples covered with thermal tape (left). 10 nm of HfO₂ was deposited at the 120 °C and the deposition cycle was repeated for 100 times. To calibrate the HfO₂ recipe of ALD, 30 nm of HfO₂ was deposited on silicon substrate as reference sample. To make sure the thickness of the HfO₂, SEM images were taken after using focused ions beam milling for the cross section. Gold layer was deposited on top of the HfO₂ to induce contrast between silicon substrate and HfO₂ for better imaging (Fig. 3.6 (right)).



Figure 3.5 The ALD machine situated at Lee nano-optics lab at Baylor science building.

The average thickness of the HfO_2 was confirmed ~ 30 nm and calibrated the HfO_2 recipe. I also measured the thickness of HfO_2 by fitting the raw data with Cauchy n-k model in the ellipsometry.

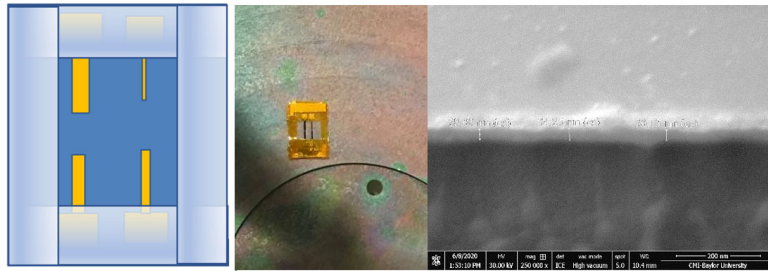


Figure 3.6 (Left) Schematic of sample with tape, (middle) the image of the sample with thermal tape and (right) the SEM image of 30 nm HfO_2 .

3.1.3 Deposition of Bottom Electrodes

At the 5th final step (Fig. 3.2) of the fabrication, 150 nm of Au was deposited by sputtering with metal mask. Before the deposition, all the masks were sonicated. The mask was rotated 90 degree with respect to the bottom electrodes. Again, before Au deposition, 10 nm of Cr was deposited at room temperature. For the Au deposition the

deposition condition was like bottom Au electrode except the deposition time. The pre-deposition time was 30 seconds after the ignition of the plasma from the Au target the main shutter was opened, and the deposition time was 900 seconds. Figure 3.7 shows the schematic diagram of the heterostructure and the optical image of one of the fabricated samples.



Figure 3.7 (Left) Schematic diagram of sample and (right) the optical image of the sample.

3.2 Optical Characterization of the ITO

For the optical characterization, the ENZ wavelength of ITO was measured by ellipsometry. The ITO was deposited on the bare silicon by magnetron sputtering with same deposition condition. For measuring the ENZ wavelength, the reflection mode of the ellipsometry was used wavelength light from 400-1700 nm incidence on the sample. The data were averaged by 5 times. Different incident angles were used for different measurements.

Drude-Lorentz model with two oscillators was used to fit the data. Two nanometers of SiO₂ in between Silicon and ITO was considered. The ENZ wavelength of ITO was confirmed at 1651 nm which is consistent with the published value. In addition, the fitted thickness of the ITO is consistent with the expected thickness measured with

profilometer. The goodness of all the fittings were almost 0.99. Table 3.1 summaries the measured ENZ wavelength of the ITO.

Table 3.1. The ENZ wavelength of ITO measured by ellipsometry.

Substrate	Angle degree	Model	ENZ wavelength nm	Thickness nm
Bare Si	55	Lorentz with two Oscillators	1651~1657	50.064

Fig. 3.8 show the real (green curves) and imaginary (red curve) part of the permittivity against the wavelength of the ITO. The real part of the permittivity goes to zero at the wavelength 1651nm. At the higher frequency or the shorter wavelength, the permittivity which is entirely real and is close to 4. This value is consistent with the characteristic of ITO described by Drude model. The imaginary part of the permittivity at the ENZ wavelength is around 1.2.

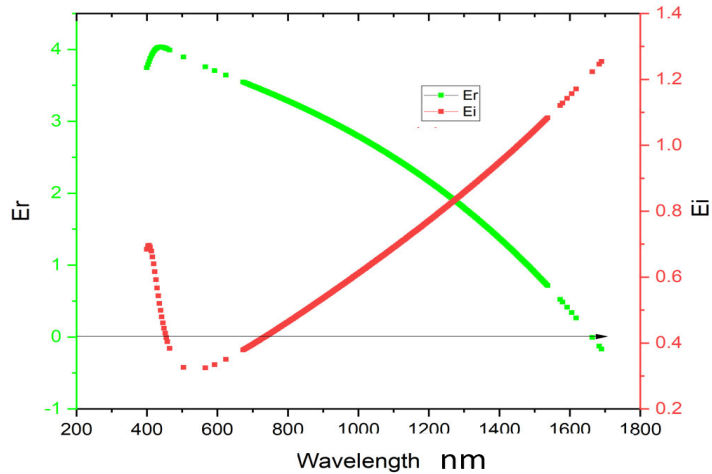


Figure 3.8 Ellipsometry measured permittivity of 50 nm thick ITO thin film.

CHAPTER FOUR

Electrical Measurement of Au/HfO₂/ITO Heterostructure

Electrical characterization is another essential part of this research. As we discussed earlier that we want to fabricate electrically drive ITO based heterostructure for SPP excitation. Therefore, we performed electrical measurements to confirm the insulating layer has good insulating property. In this chapter, the electrical characterization of the fabricated heterostructure will be presented.

4.1 Electrical Measurement

In the previous chapters, we have discussed about the mechanism and fabrication of Glass/Au/ HfO₂/ITO heterostructure. Our goal is to observe ENZ emission from the ENZ heterostructure. To confirm the electron tunnelling mechanism, we need to observe the breakdown voltage of HfO₂. Breakdown voltage is an electrical property of the material and it is the maximum voltage at which the insulator is electrically breakdown (current pass through the Au/ITO layer). There are several ways to measure the breakdown voltage. We used Keithely-4250 semiconductor analyzer with probe station which is situated at BRIC facility of Baylor university (Fig. 4.1). As a part of electrical measurement, different samples have been measured.

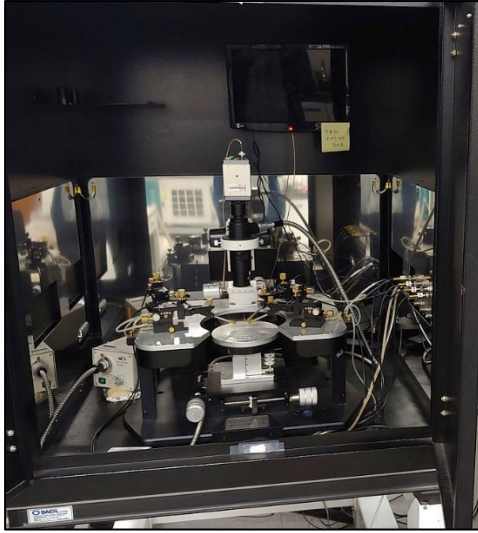


Figure 4.1 The probe station with Keithley-4200 semiconductor analyzer.

4.2 Breakdown Voltage of HfO₂

Throughout the study of the breakdown voltage, we can know the maximum voltage that we can apply to an insulator until the insulator becomes conductive. Several samples of Au/HfO₂/Au were used to measure the breakdown voltage of HfO₂. We used the probe station with semiconductor analyzer to measure the breakdown voltage. The samples were fabricated with the similar deposition condition discussed in chapter three. The thickness of HfO₂ was 10 nm and Au was 50 nm also like the main samples. In the Fig. 4.2 the schematic diagram of extra sample has been showed with defining the device areas.

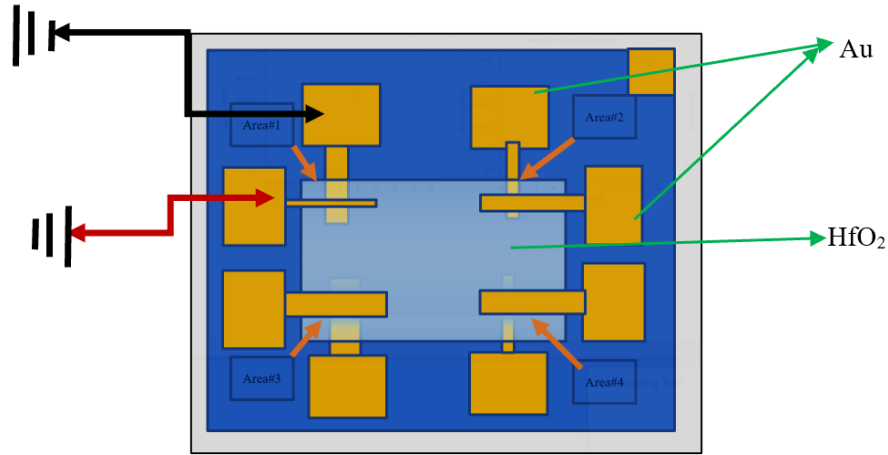


Figure 4.2 The Schematic diagram with probe.

The two probes were connected to the bottom and top Au electrodes as shown in the Fig. 4.2. When the voltage was applied, the electron started to flow from the positive (bottom electrode) to negative (top electrode) direction. Due to the insulation of HfO₂, the current cannot flow like a conductor. However, at a certain voltage, insulator will electrically break down and hence current could flow between top and bottom electrodes. Voltage sweep mode from 0V to 16V was applied to examine the breakdown voltage.

In the Fig. 4.3, the non-linear I-V curves have been shown of From the figures, we can see that the current is low when the applied voltage is below 7 V. In this region the resistance is very high due to the insulating layer. After a certain voltage, the current suddenly rise sharply and then continues till maximum voltage 20V. For the sample#1 the breakdown volage of the four device areas are 7.35, 7.55 V respectively. These values of breakdown voltages are consistent with the other published work [19] on HfO₂ deposited by ALD. The breakdown voltages of other three samples were summarized in the table 4.1(a). From the Table 4.1(a) we can see with the changes of areas of the device the breakdown voltages also vary. As shown in Fig. 4.5, the highest breakdown voltage was

found to be 12.585 V and the lowest breakdown voltage was 6.085 V. However, in average, we observed breakdown voltages between 7-10 V. The variation of the breakdown voltages is because of the slightly different distribution of pin-hole effects and different surface conditions for different areas during the depositions.

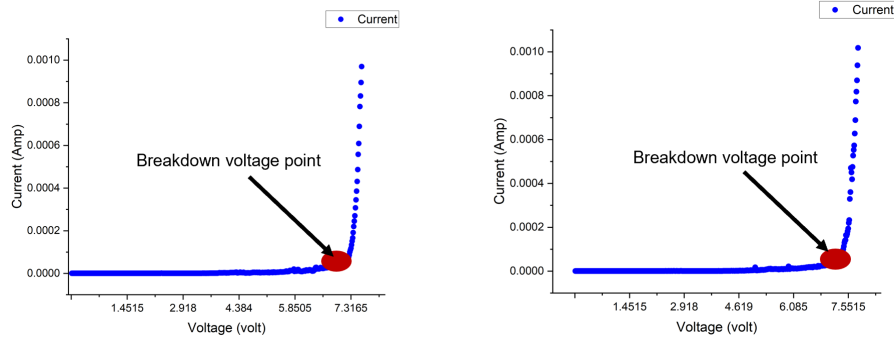


Figure 4.3 (left)The I-V curve of sample#1 area#1 ,and (right) area#2

Table 4.1 The Breakdown voltages of different areas of various samples.

Samples	Area in (μm^2)	Breakdown Voltage (V)
Sample#1 A#1	9.523×10^4	7.625
Sample#1 A#2	9.523×10^4	7.625
Sample#1 A#3	1.804×10^5	7.698
Sample#1 A#4	4.392×10^4	7.845
Sample#2 A#1	5.145×10^4	9.400
Sample#2 A#2	1.808×10^5	12.585
Sample#2 A#3	1.681×10^5	7.581
Sample#2 A#4	5.353×10^4	7.728
Sample#3 A#1	1.480×10^5	10.281
Sample#3 A#2	4.987×10^4	9.766
Sample#3 A#3	1.954×10^5	10.396
Sample#3 A#4	1.169×10^5	8.035
Sample#4 A#1	1.711×10^5	6.085
Sample#4 A#2	5.903×10^4	8.505
Sample#4 A#3	2.241×10^5	10.381
Sample#4 A#4	1.118×10^5	8.299

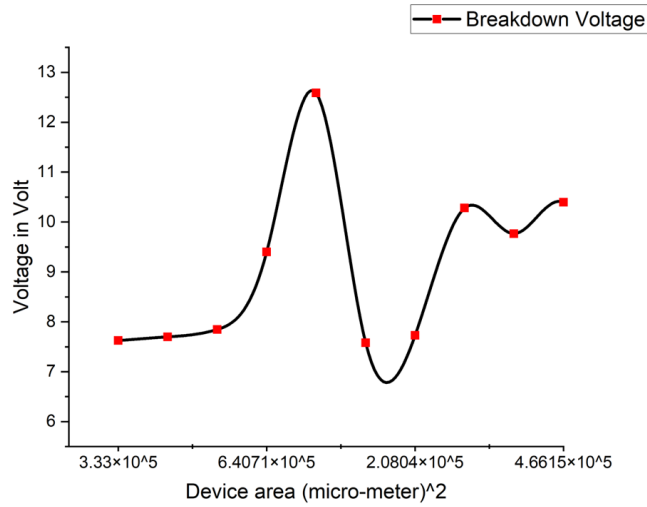


Figure 4.4 Breakdown voltages corresponding to different device areas.

4.3 The Measurement of Tunneling Current

The study of electron transport in (ENZ-I-M) heterostructures is an important part of this research work because the light generation will depend on hot electron tunneling. We will be looking at three main conduction mechanisms in an insulating thin film, namely (i) Schottky emission (SC), (ii) Poole-Frenkel emission (PF) and (iii) Fowler-Nordheim (FN) tunneling; the equations 4.1 to 4.3, respectively.

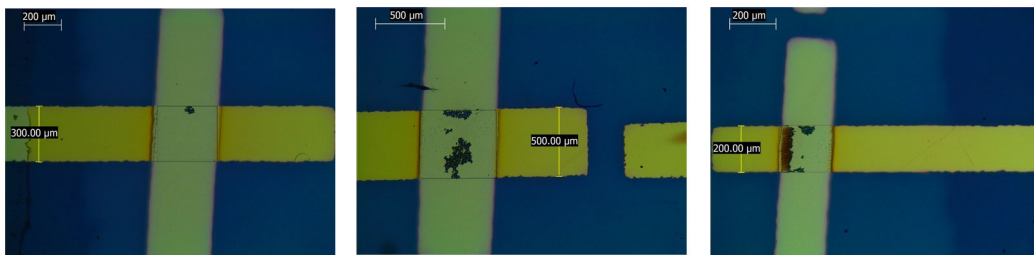


Figure 4.5 (Left) Sample#1 image of device#1, (middle) device#2, and (right) device#3.

$$J_{SC} = AT^2 \exp\left(\frac{\phi_{SC} - \beta_{SC}\sqrt{E}}{KT}\right) \dots \dots \dots (4.1)$$

$$J_{PF} = cE \exp\left(-\frac{\phi_{PF} - \beta_{PF}\sqrt{E}}{2KT}\right) \dots \dots \dots (4.2)$$

$$J_{FN} = CE^2 \exp\left(-\frac{\gamma}{E}\right) \dots \dots \dots (4.3)$$

where,

$$\beta_{SC} = \left(\frac{q^3}{4\pi\epsilon_0\epsilon_r}\right)^{\frac{1}{2}} \dots \dots \dots (4.4)$$

$$\beta_{PF} = \left(\frac{q^3}{\pi\epsilon_0\epsilon_r}\right)^{\frac{1}{2}} \dots \dots \dots (4.5)$$

$$\gamma = [8\pi(2m^*)^{\frac{1}{2}}(\phi_{FN})^{\frac{3}{2}}]/3qh \dots \dots \dots (4.6)$$

Here, q is electron charge, h is Planck's constant, K is Boltzmann's constant, m^* is effective mass of electron, J_{sc} is the Schottky current, J_{PF} is PF current, J_{FN} is FN tunneling current, E is the applied electric field, ϵ_0 is the permittivity at vacuum, ϵ_r is the dielectric constant of an insulator (HfO₂), and ϕ_{FN} is the FN tunneling barrier height. To reveal the PF conduction, $\ln J/E$ is plotted against \sqrt{E} . A linear dependence at moderate electric fields is the PF emission, i.e., electron transport between localized trap states in HfO₂ (Fig. 4.6). The slope of the linear regression gives the value of $\beta_{PF} / 2kT$ in equation (4.2). β_{PF} can be calculated from equation (4.4). After simple math, the dielectric constant ϵ_r of HfO₂ is found. The value is 15 which is close to values reported in the literature for thin HfO₂ films.

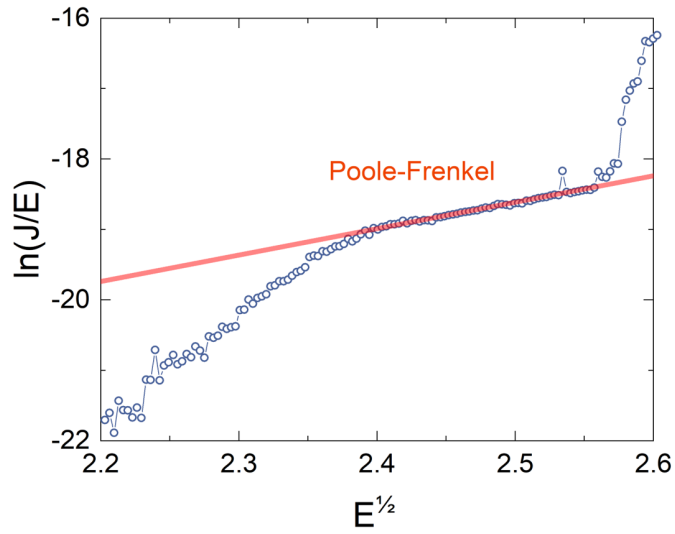


Figure 4.6 The PF emission current at moderate electric field.

The FN tunneling under high applied electric field is shown in the Fig. 4.7. The horizontal and the vertical axes are the reciprocal of electric field and $\ln(J/E^2)$, respectively. The red line shows a linear regression through the experimental points, which supports FN tunneling current at high electric fields. From the slope of the linear regression, we obtained a height of the tunneling barrier of 2.7 eV.

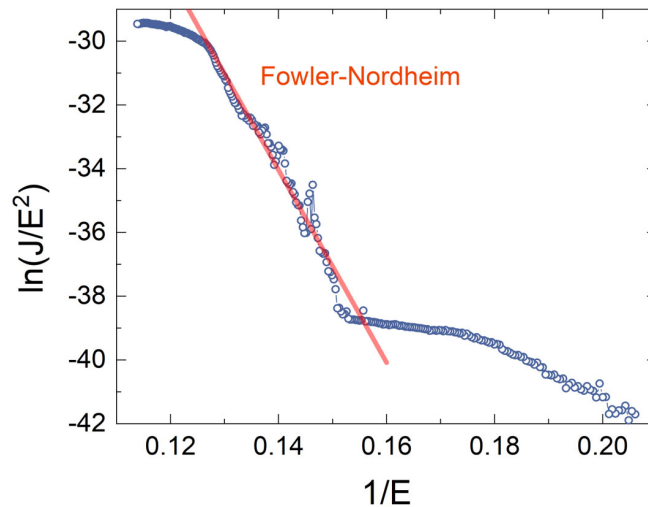


Figure 4.7 The FN tunneling current at the higher electric field.

In summary, the Fowler-Nordheim tunneling is observed in the ITO/HfO₂/Au heterostructure under high electrical bias, which is important for the light generation from the heterostructure. The dielectric constant of HfO₂ obtained from the Poole-Frenkel electron emission at moderate bias is consistent with the literature reported values [19,20].

CHAPTER FIVE

Optical Characterization, Result and Discussion

One of the goals of this project is to examine the electrically induced light emission in the ENZ heterostructure. To detect the ENZ emission from the heterostructure, free-space optical measurement setup is used to detect the optical signal with electrical bias to the samples.

5.1 Optical Measurement

One of the goals of this project is to examine the electrically induced light emission in the ENZ heterostructure. To detect the ENZ emission from the heterostructure, Free space optical measurement setup I need to detect the optical signal and at the same time applying the electrical bias to the samples.

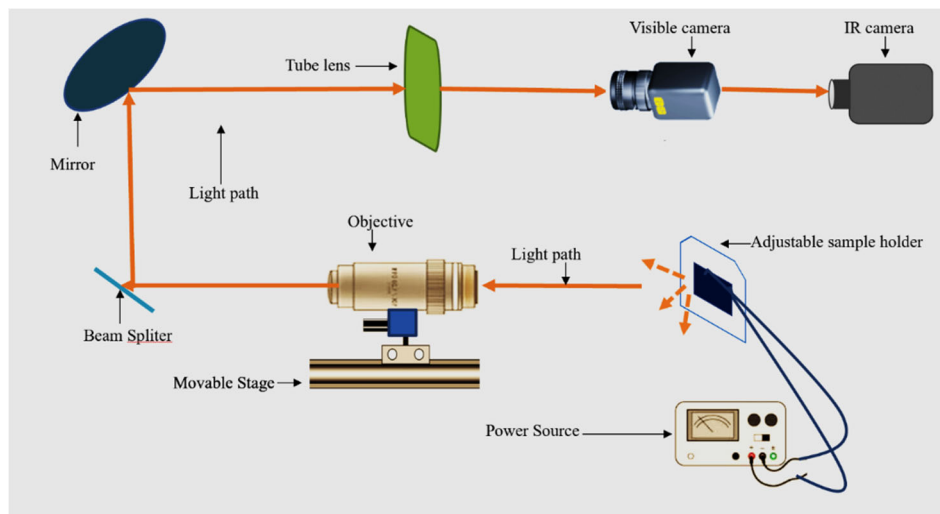


Figure 5.1 Schematic diagram of the optical setup to detect the emission of light.

To perform optical measurements with sample holder in the electrical holder and connecting wires, a 50x long-distance objective lens with working distance of 17 mm, effective focal length of 4.0 mm, and numerical aperture of 0.42 has been used to image the device. The objective is mounted on a movable stage that can move in the X, Y and Z directions. Mirror, beam splitter, and tube lens are used to collimate the emitted beam to the visible or NIR camera for collecting the images. Visible light source is launched from the beam splitter such that the active device area could be properly located for the light emission (similar function as an optical microscope).

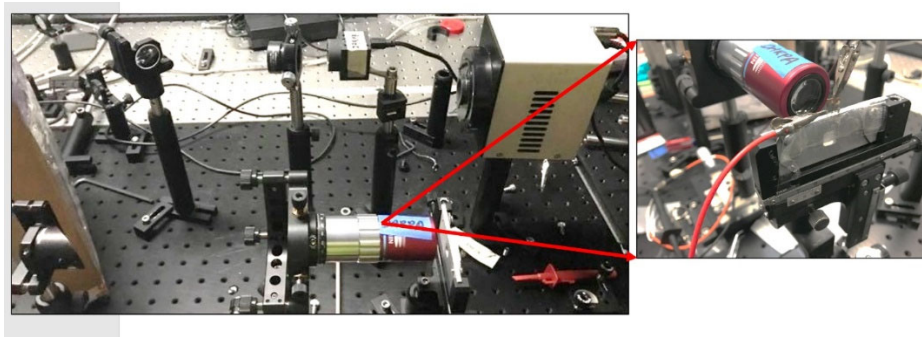


Figure 5.2 (left)The picture of the optical set up, and (right) the sample with sample holder.

5.2. Electrical connection in optical measurement setup

The main challenge was to apply the voltage to the samples while the samples are in the compact optical setup. To solve this issue, I used Keithley-2450 power source and used small alligators' clips to make the connection in between samples and power source. However, using alligator clips to the sample's electrode pads could damage the electrode pads and for this reason I used Ag paste to electrically connect with the electrode pads. The Ag paste provides external space to connect the clips to the samples. To make sure the Ag paste connection works well and does not provide external resistance to the device, I

fabricated 200 nm of Au by sputtering on the glass substrate using the same deposition condition described in the chapter three.

The I-V curve of the test sample was measured with both probe station and Keithley-2450 power source. In both cases the I-V curves were measured with and without Ag paste.

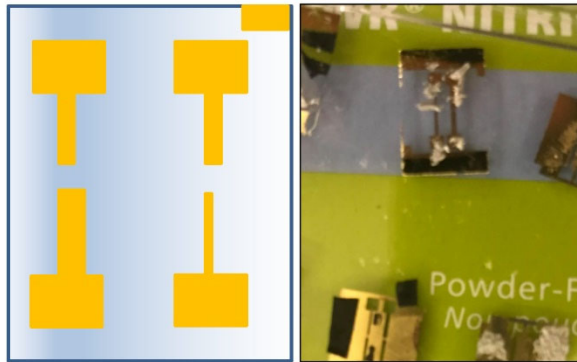


Figure 5.3 (Left) The schematic of test sample and (right) the picture of the test sample.

The I-V curve was measured with probe station with Ag paste (Fig. 5.4). The I-V curves in Fig 5.4 (a-d) represented the four electrodes of the test sample. The I-V curve show ohmic characteristic because the Au electrode is good conductor.

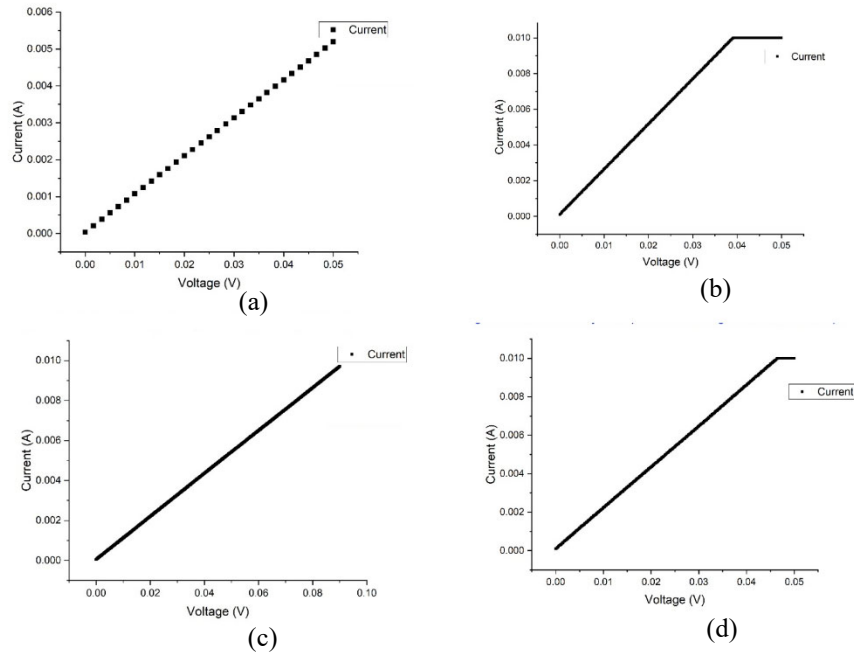


Figure 5.4 The I-V curve of (a) first electrode, (b) second electrode, (c) third electrode, and (d) fourth electrode of test sample.

The resistances calculated from these I-V curves of four electrodes with Ag paste are 9.61, 3.92, 9.26 and 4.24 ohm, respectively. Without the Ag paste the I-V curve of test sample was also measured and the calculated resistance is 4 ohms. From these two measurements, the average contribution from Ag paste was found to be only 2.80 ohm. The measurements are summarized in the Table 5.1.

Table 5.1 Measurement with Probe Station for four different electrodes.

Measurement	R Without Everything Ohm	R With Ag Paste Ohm	Ag Paste Resistance Ohm
Electrode 1	4	9.61	5.61
Electrode 2	4	3.94	0.06
Electrode 3	4	4.24	0.24
Electrode 4	4	9.26	5.26

Again, the same measurement was repeated by using the Keithley-2450 power source with the Ag paste and without Ag paste. In the Fig 5.5 the graph (a-c) showed the I-V curve of three electrodes with Ag paste by Keithley-2450.

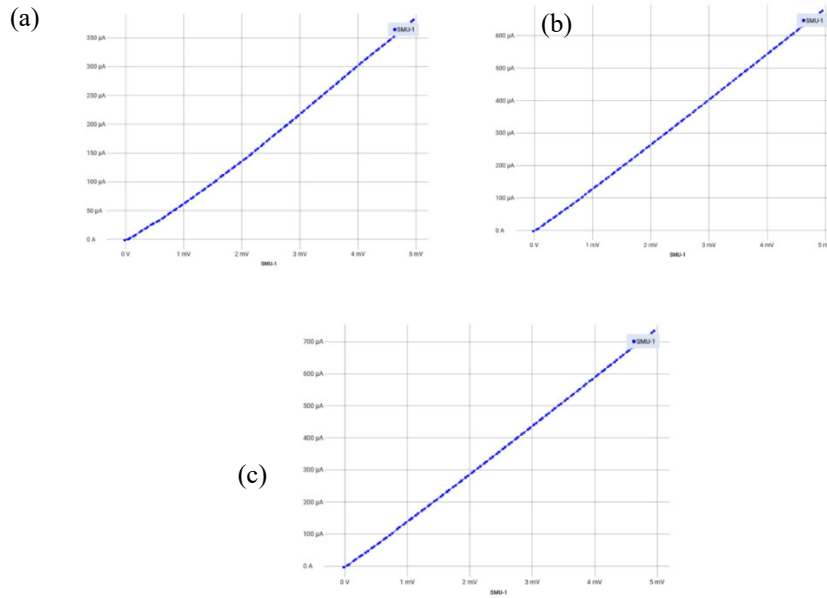


Figure 5.5 The I-V curve of (a) first electrode, (b) second electrode, and (c) third electrode of test sample by Keithley-2450 with Ag paste.

From the I-V curve, the measured resistances of three Au electrodes are 13.02, 7.32, and 6.75 ohms, respectively. I also measured the Au electrodes by Keithley-2450 without Ag paste and found the resistance is 3.92 ohm (Table 5.2). Finally, from these two measurements, the average resistance of the Ag paste by the Keithley-2450 is 5.11 ohm.

Table 5.2 Measurement with Keithley-2450

Measurement	R Without Everything Ohm (probe)	R With Ag and Clips Ohm	Ag Paste and Clips Resistance Ohm
Electrode 1	3.92	13.02	9.1
Electrode 2	3.92	7.32	3.4
Electrode 3	3.92	6.75	2.83

The measured Ag paste resistance from Keithley-2450 and probe station is 5.11 ohm and 2.80 ohm, respectively. This contribution is negligible compared to the resistance with our ITO-I-M heterostructure. Therefore, we confirm that the samples could be electrically connected with Ag paste and alligator clips.

5.3 Conclusions

We have fabricated ITO/HfO₂/Au ENZ heterostructures with precise thickness and geometry. The ITO thin films have ENZ wavelength from 1625-1700 nm measured with ellipsometry technique. In the electrical characterization, breakdown voltage is 7-9 Volts of 10 nm-thick HfO₂ thin film, showing a good insulating property. The breakdown voltage also defines the maximum voltage that we can apply to the samples. Moreover, the existence of tunneling current has also been confirmed by analyzing the IV characteristics. The analysis showed that the fabricated heterostructures have the Fowler-Nordheim electron tunneling. This tunneling mechanism is important for exciting the ENZ mode and light emission. The optical setup is also built to observe the light emission.

5.3.1 Expectations and Perspectives

We are currently performing optical measurements of the ITO/HfO₂/Au ENZ heterostructures with expectation of light emission enhancement in the NIR spectrum range close to the ENZ wavelength. We will further investigate the tunneling current mechanism from the heterostructure. We will design the heterostructure's geometry, such as thin film thicknesses, and ENZ wavelength for enhanced electrically induced light emission.

REFERENCES

- [1] Koller, D., Hohenau, A., Ditlbacher, H. et al. Organic plasmon-emitting diode. *Nature Photon* 2, 684–687 (2008).
- [2] Neutens, P., Lagae et al. Electrical excitation of confined surface plasmon polaritons in metallic slot waveguides. *Nano Lett.*, 10, 4, 1429–1432 (2010)3.
- [3] Huang, K., Seo, M.K., Sarmiento, T. et al. Electrically driven subwavelength optical nanocircuits. *Nature Photon* 8, 244–249 (2014).
- [4] Walters, R., van Loon, R., Brunets, I. et al. A silicon-based electrical source of surface plasmon polaritons. *Nature Mater* 9, 21–25 (2010).
- [5] F. Bigourdan, et al., Nanoantenna for electrical generation of surface plasmon polaritons, *Physical Rev. Lett.* 116, 106803 (2016).
- [6] Qian, H., Hsu, S.W., Gurunatha, K. et al. Efficient light generation from enhanced inelastic electron tunnelling. *Nature Photon* 12, 485–488 (2018).
- [7] Kern, J. et al. Electrically driven optical antennas. *Nat. Photon.* 9, 582–586 (2015).
- [8] Parzefall, M. et al. Antenna-coupled photon emission from hexagonal boron nitride tunnel junctions. *Nat. Nanotech.* 10, 1058–1063 (2015).
- [9] Wei Du, et al. Highly efficient transducers, *nature photonics*, vol 11, 623-637, 2017.
- [10] Veselago V G, The electrodynamics of substances with simultaneously negative values of ϵ and μ , *Sov. Phys. Usp.* 10 509–514 (1968).
- [11] X. Niu et al, ENZ photonics: a new platform for integrated devices, *Optical Mater*, 6, 17012092, (2018).
- [12] S. Campione et al, “Electric field enhancement in ENZ slabs”, *Physical Review B* 87, 035120 (2013).
- [13] Yoon, J. et al. Broadband Epsilon-Near-Zero Perfect Absorption in the Near-Infrared. *Sci. Rep.* 5, 12788 (2015).

- [14] Badsha et.al, Admittance matching analysis of perfect absorption in ultra-thin, unpatterned films. *Opt. Commun.* 332, 206–213 (2014).
- [15] A. Anopchenko et.al, Field-Effect Tunable and Broadband Epsilon-Near-Zero Perfect Absorbers with Deep Subwavelength Thickness, *5*, 2631–2637 (2018).
- [16] Kinsey, N., DeVault, C., Boltasseva, A. et al. Near-zero-index materials for photonics. *Nat Rev Mater* 4, 742–760 (2019).
- [17] H. Lee et.al., Nanoscale conducting oxide PlasMOSTor, *Nano Lett.* 14, 6363–6468 (2014).
- [18] Sorger, Volker et.l. "Ultra-compact silicon nanophotonic modulator with broadband response" *Nanophotonics*, vol. 1, no. 1, 2012, pp. 17-22.
- [19] David I Shahin. et.al, Electrical characterization of ALD HfO₂ high-K dielectric Ga₂O₃, *Appl. Phys. Lett.* 112, 042107, (2018).
- [20] Koller, D., Hohenau, A., Ditlbacher, H. et al. Organic plasmon-emitting diode. *Nature Photon* 2, 684–687 (2008).
- [21] Neutens, P., Lagae et. al. Electrical excitation of confined surface plasmon polaritons in metallic slot waveguides. *Nano Lett.*, 10, 4, 1429–1432 (2010)3. Huang, K., Seo, MK., Sarmiento, T. et al. Electrically driven subwavelength optical nanocircuits. *Nature Photon* 8, 244–249 (2014).
- [22] 4. Walters, R., van Loon, R., Brunets, I. et al. A silicon-based electrical source of surface plasmon polaritons. *Nature Mater* 9, 21–25 (2010).
- [23] J.F. Conley, et.al. Electrical properties of deposited via atomic layer deposition using H₂O and Hf(NO₃)₄ *Appl. Phys. Lett.* 82, 3508 (2003).